Fine-structure electric-dipole matrix elements of He-like ions for x-ray line-shape calculations

F. B. Rosmej,* B. Deschaud, and K. Bennadji
Sorbonne University, Pierre and Marie Curie, LULI, UMR 7605, case 128, 4 place Jussieu, 75252 Paris Cedex 05, France and LULI, Ecole Polytechnique, CNRS, CEA, Physique Atomique dans les Plasmas Denses-PAPD, Palaiseau 91128, France

P. Indelicato
Sorbonne University, Pierre and Marie Curie, LKB, UMR 8552, case 74, 4 place Jussieu, 75252 Paris Cedex 05, France and ENS, École Normale Supérieure, 24 rue Lhomond, 75231 Paris Cedex 05, Paris, France

J. P. Marques
Departamento de Física, Centro de Física Atómica, Faculdade de Ciências, Universidade de Lisboa, Campo Grande, Edifíco C8, Lisboa 1749-016, Portugal

(Received 17 October 2012; published 27 February 2013)

Dipole matrix elements have been calculated with different methods in the intermediate-coupling scheme to study their impact on the Stark effect of highly charged ions. Special emphasis has been devoted to the $1s3l$ fine structure of He-like ions that is widely employed for Stark broadening analysis in dense plasmas. Apart from a wavelength shift in the total He_β group in the x-ray energy range, important differences in the Stark width, induced line dips, and relative intensities of maxima are demonstrated for different methods of calculation. We found that these differences were related to the precision of the fine-structure dipole matrix elements and related wavelengths and explored the particularities of atomic structure precision for line broadening purposes that was distinct from the current database approaches. Based on advanced multi-configuration-Dirac-Fock simulations, we propose a complete set of high-precision matrix elements and wavelengths. Detailed numerical results are presented for He-like aluminum. We also discuss the influence of relativistic approximations in atomic structure on the line broadening.

DOI: 10.1103/PhysRevA.87.022515 PACS number(s): 31.15.ac, 32.30.Rj, 32.60.+i

I. INTRODUCTION

The Stark effect had successfully been introduced to plasma spectroscopy more than 50 years ago and since then, has become an important standard diagnostics for the density determination [1–4]. Line broadening covers almost 20 orders of magnitude in density, ranging from low-density astrophysical plasmas to above solid density plasmas for compressed fuels in inertial fusion science. Due to this huge density range and the possibility of employing a large variety of diagnostic test elements (either intentionally inserted as tracer elements or presented as intrinsic elements), charge states, and principal quantum numbers, line broadening in plasmas has become a very interdisciplinary science.

Line broadening theory was originally applied to lines originating from single excited states but also has been transferred to the autoionizing states $2l2l'$, $1s2l2l'$, and $1s2l3l'$ [5,6]. Powerful methods have been developed [6–11] that employ a generalized atomic structure input (energies and reduced matrix elements) for broadening calculations of very complex configurations. This has opened up the possibility for advanced studies of matter under extreme conditions via the analysis of autoionizing states [12]. Also, the investigation of quantum-mechanical interference effects via transitions of hole states induced by free-electron XUV or x-ray lasers via photoionization of inner shells now seems possible [13,14].

Although, today, databases (e.g., Ref. [15] and related Refs. [16–20]) have greatly improved the accessibility of atomic data for various ions and atoms (transition probabilities and, in particular, energy levels), Stark profile calculations request particular supplementary information that usually cannot be extracted either from the databases or from the experiments. The example of the He_β transition group of highly charged ions might illustrate this circumstance: Databases provide the transition wavelength and transition probability for the $1s3p\ ^1P_1$-$1s^2\ ^1S_0$ transition, however, the electric field mixes the $1s3d\ ^1D_2$ and $1s3p\ ^1P_1$ states via the dipole matrix element $\langle 1s3d\ ^1D_2|r|1s3p\ ^1P_1\rangle$. This results in a Stark transition $1s3d\ ^1D_2$-$1s^2\ ^1S_0$. It is difficult to measure the dipole matrix element $\langle 1s3d\ ^1D_2|r|1s3p\ ^1P_1\rangle$ directly, and databases do not provide information either. Therefore, essential data for Stark broadening calculations are missing, and the line profile calculation relies almost entirely on theoretical atomic structure calculations (as far as the important Stark coupling is concerned). We note that transition energies for the fine-structure matrix elements could be deduced from a complete set of energy levels that are provided by databases for some elements and simple configurations, however, these are data that are also either calculated or not available (in particular, for many electron systems and autoionizing states).

It is the aim of the present paper to critically analyze the current situation of atomic structure calculations for Stark broadening applications. Based on sophisticated relativistic atomic structure calculations, we propose a benchmark set of energy levels, transitions energies, and dipole matrix elements and compare them with widely employed atomic structure codes and methods.

*frank.rosmej@upmc.fr

II. FINE-STRUCTURE DIPOLE MATRIX ELEMENTS AND ELECTRIC-FIELD EFFECTS

The interaction of the electric field E with the atom requests the calculation of matrix elements with the electric-field Hamiltonian. In the dipole approximation, the matrix elements can be expressed in terms of the reduced dipole matrix element (energies are in units of $e/2a_0^2$),

$$\langle \gamma J M|H_{\rm elec}|\gamma' J' M'\rangle = -2E(-1)^{J-M}\begin{pmatrix} J & 1 & J' \\ -M & 0 & M' \end{pmatrix}\langle \gamma J\|r\|\gamma' J'\rangle. \quad (1)$$

The dipole transition matrix element $\langle \gamma J M|r_q|\gamma' J' M'\rangle$ is related to the reduced matrix $\langle \gamma J\|r\|\gamma' J'\rangle$ via the Wigner-Eckart theorem,

$$\langle \gamma J M|r_q|\gamma' J' M'\rangle = (-1)^{J-M}\begin{pmatrix} J & 1 & J' \\ -M & q & M' \end{pmatrix}\langle \gamma J\|r\|\gamma' J'\rangle. \quad (2)$$

The spontaneous transition probability A is given by

$$A_{J'J} = \frac{64\pi^4 e^2 a_0^2}{3h\lambda^3}|\langle \gamma J\|r\|\gamma' J'\rangle|^2 \sum_{Mq}\begin{pmatrix} J & 1 & J' \\ -M & q & M' \end{pmatrix}^2 = \frac{64\pi^4 e^2 a_0^2}{3h\lambda^3 (2J'+1)}|\langle \gamma J\|r\|\gamma' J'\rangle|^2, \quad (3)$$

$$A_{J',J} = \frac{2.0261\times 10^{-12}}{(2J'+1)\lambda^3}S_{J,J'} = \frac{6.6702\times 10^{-5}(2J+1)}{(2J'+1)\lambda^2}f_{J,J'} \quad (4)$$

where λ's are the wavelengths in $[m]$, $f_{J,J'}$ is the oscillator strength, and $S_{J,J'}$ is the line strengths (in units of $e^2 a_0^2$) that is given by

$$S = |\langle \gamma J\|r\|\gamma' J'\rangle|^2, \quad (5)$$

and its relation to the oscillator strength via

$$f_{J,J'} = \frac{8\pi^2 m_e c a_0^2}{3h(2J+1)\lambda}|\langle \gamma J\|r\|\gamma' J'\rangle|^2. \quad (6)$$

We note that the reduced matrix elements Eq. (1) cannot generally be deduced from the spontaneous transition probabilities Eq. (3) because the reduced matrix element contains a sign.

In plasmas, the electric microfield distribution of ions and electrons requests the consideration of a large number of electric-field values. The Hamiltonian has to be diagonalized for each electric-field value; this is a complex and very time-consuming task. In order to avoid direct numerical calculation of, e.g., the Schrödinger equation (implying the calculation of wave functions, etc.), transforming the problem to reduced matrix elements has been proposed [7–11]. In this approach, atomic structure calculations of energy levels and all possible dipole matrix elements serve as an external input to the final Stark profile calculations. Combined with the frequency fluctuation method [8,9], this separation considerably reduces the numerical burden that allows treating complex configurations. Even simulations for transitions in hollow ions [12] and interference effects of autoionizing states [13,14] become possible on simple workstations.

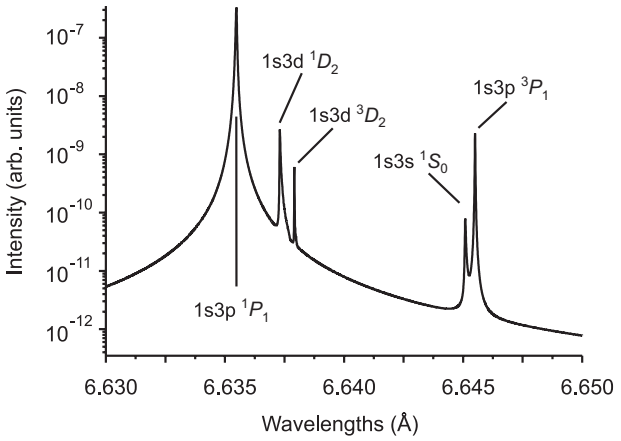

FIG. 1. He_β Stark profile of aluminum showing different electric-field-induced transitions $kT_e = 100$ eV and $n_e = 10^{20}$ cm^{-3}.

Our primary concern is the He_β emission of highly charged He-like ions that are widely used in high-density plasma diagnostics [6,21,22]. Moreover, the simplicity of the $1s3l$ fine structure allows transparent discussion of all essential Stark broadening effects. Figure 1 shows the Stark broadening calculations for the He_β emission of He-like aluminum. The selected moderate density of $n_e = 10^{20}$ cm^{-3} allows identifying the relevant Stark coupling via the fine-structure matrix elements $\langle 1s3l\ ^{2S+1}L_J|r|1s3l'\ ^{2S'+1}L'_{J'}\rangle$ that are not yet masked too much by a large number of overlapping transitions. It can be clearly seen that the electric-field effect induces the transitions $1s3d\ ^1D_2$-$1s^2\ ^1S_0$ and $1s3s\ ^1S_0$-$1s^2\ ^1S_0$. As intermediate-coupling effects are included in the atomic structure calculations, we also encounter the transitions from the triplet system: $1s3p\ ^3P_1$-$1s^2\ ^1S_0$ is the usual intercombination line, and $1s3d\ ^3D_2$-$1s^2\ ^1S_0$ is induced by the electric field. The transition $1s3s\ ^3S_1$-$1s^2\ ^1S_0$ is rather weak and outside the spectral interval depicted by Fig. 1. Figure 1 (and also the following figures) presents the Stark broadening calculations carried out with the PPP code [8,10]. The simulations demonstrate that not only is the resonance wavelength $1s3p\ ^1P_1$-$1s^2\ ^1S_0$ important for the overall distribution of the broadening effects, but also are transitions from the $1s3s$ and $1s3d$ levels. Therefore, the complete set of energy levels in the fine-structure $1s3l$ is important together with its related dipole matrix elements.

Table I compares various atomic data that have been calculated with different methods and codes, indicated as "MCDFGME," "HFR," "FAC," and "MZ." The second column indicates the atomic transition, the third column indicates the corresponding wavelength, and the fourth column indicates the related oscillator strength (being proportional to the square of the reduced matrix element). As for nonhydrogenic ions, the Stark effect is quadratic with an energy shift given by

$$\Delta E_\alpha \approx E_Z^2 \sum_{\alpha\neq\alpha'}\frac{|\langle n\alpha'|\vec{d}|n\alpha\rangle|^2}{E_{n\alpha}-E_{n\alpha'}} = E_Z^2 \sum_{\alpha\neq\alpha'}\frac{|\langle n\alpha'|\vec{d}|n\alpha\rangle|^2\lambda_{\alpha\alpha'}}{hc}, \quad (7)$$

in the fifth column, Table I presents the product of the oscillator strengths and the squares of the corresponding wavelengths [see Eq. (6)].

TABLE I. Selected wavelengths and electric-dipole oscillator strengths related to the $1s3l$ fine structure of He-like aluminum ions. The first values are calculated with the MCDFGME method, the second values are calculated with HFR, the third values are calculated with FAC, and the fourth values are calculated with MZ, see text. Transitions of Nos. 3, 4, 10, and 12 also indicate the values from NIST [15–20].

Number	Transition	$\lambda(10^{-10}$ m)/$\Delta\lambda(10^{-13}$ m)	f_{E1}	$f_{E1}\,\lambda^2$
1	$1s^2\ {}^1S_0$-$1s3s\ {}^1S_0$	6.6451/ −9.6		
		6.6434/ −9.5		
		6.6481/ −10.0		
		6.6444/ −9.7		
2	$1s^2\ {}^1S_0$-$1s3s\ {}^3S_1$	6.6585/ −23.0		
		6.6571/ −23.2		
		6.6618/ −23.7		
		6.6576/ −22.9		
3	$1s^2\ {}^1S_0$-$1s3p\ {}^1P_1$	6.6355/ ± 0	1.505×10^{-1}	6.626
		6.6339/ ± 0	1.631×10^{-1}	7.178
		6.6381/ ± 0	1.515×10^{-1}	6.676
		6.6347/ ± 0	1.524×10^{-1}	6.709
		NIST: 6.6348	1.506×10^{-1}	6.630
4	$1s^2\ {}^1S_0$-$1s3p\ {}^3P_1$	6.6455/ −10.0	4.546×10^{-4}	2.008×10^{-2}
		6.6442/ −10.3	3.642×10^{-4}	1.608×10^{-2}
		6.6485/ −10.4	4.012×10^{-4}	1.610×10^{-2}
		6.6447/ −10.0	4.627×10^{-4}	2.043×10^{-2}
		NIST: 6.6447		
5	$1s^2\ {}^1S_0$-$1s3d\ {}^1D_2$	6.6373/ −1.8		
		6.6362/ −2.3		
		6.6407/ −2.6		
		6.6364/ −1.7		
6	$1s^2\ {}^1S_0$-$1s3d\ {}^3D_2$	6.6379/ −2.4		
		6.6368/ −2.9		
		6.6413/ −2.6		
		6.6370/ −2.3		
7	$1s3s\ {}^1S_0$-$1s3p\ {}^1P_1$	4.5968×10^3	7.416×10^{-2}	1.567×10^6
		4.6086×10^3	7.362×10^{-2}	1.564×10^6
		4.4506×10^3	7.560×10^{-2}	1.497×10^6
8	$1s3s\ {}^3S_1$-$1s3p\ {}^3P_2$	3.2375×10^3	5.722×10^{-2}	5.997×10^5
		3.2392×10^3	5.730×10^{-2}	6.012×10^5
		3.1872×10^3	5.886×10^{-2}	5.979×10^5
9	$1s3p\ {}^3P_1$-$1s3s\ {}^1S_0$	1.0447×10^5	3.194×10^{-6}	3.486×10^4
		6.0316×10^4	4.183×10^{-6}	1.522×10^4
		9.1732×10^4	3.312×10^{-6}	2.787×10^4
10	$1s3d\ {}^1D_2$-$1s3p\ {}^1P_1$	2.4354×10^4	3.222×10^{-3}	1.911×10^6
		1.8659×10^4	4.277×10^{-3}	1.489×10^6
		1.7467×10^4	4.579×10^{-3}	1.397×10^6
		NIST: 2.6525×10^4		
11	$1s3p\ {}^3P_1$-$1s3d\ {}^3D_2$	5.8105×10^3	1.719×10^{-2}	5.804×10^5
		6.0006×10^3	1.692×10^{-2}	6.092×10^5
		6.1206×10^3	1.648×10^{-2}	6.174×10^5
12	$1s3d\ {}^3D_2$-$1s3p\ {}^1P_1$	1.8178×10^4	3.636×10^{-4}	1.201×10^5
		1.4944×10^4	3.490×10^{-4}	7.794×10^4
		1.3849×10^4	3.948×10^{-4}	7.572×10^4
		NIST: 1.9581×10^4		

The first method, MCDFGME, is developed in the present paper and is proposed as a benchmark. It employs the multiconfiguration Dirac-Fock code of Desclaux [23] and Desclaux and Indelicato [24], and it includes QED corrections to compute energies, wave functions, spontaneous radiative transition probabilities, and corresponding matrix elements. Details on the Hamiltonian and the construction of the wave functions are described elsewhere [23,25–27]. For the radiative transition probabilities and reduced matrix elements, the code implements exact relativistic formulas [23,28–31].

For these transitions, the so-called optimized levels method was used to determine the wave function and energy for each

state involved. This method allows for a full relaxation of both initial and final states, providing much better energies and wave functions. However, spin orbitals in the initial and final states are not orthogonal since they have been optimized separately. To account for the wave-functions' nonorthogonality, the code uses the formalism described by Löwdin [32]. For the present calculations, the nonrelativistic configurations ($1s^2 + 2s^2 + 2p^2$), $1s2s$, $1s2p$, $1s3s$, $1s3p$, $1s3d$, $1s4s$, $1s4p$, $1s4d$, $1s4f$, $1s5s$, $1s5p$, $1s5d$, $1s5f$, $1s5g$, $1s6s$, $1s6p$, $1s6d$, $1s6f$, $1s6g$, and $1s6h$ are selected to construct initial wave functions. From the comparison of our calculated wavelengths with other available data, we estimate that they are precise to less than 1% and to a maximum of 10% for the transition probabilities and Stark matrix elements of the fine structure. The later value was based on the difference of the length and velocity form values for the transition probabilities and a comparison with observed and calculated data presented in the National Institute of Standards and Technology (NIST) atomic spectra database [15–20]. The main source of this uncertainty is the omission of the electronic correlation in the wave functions of the excited levels.

The second method, HFR, employs the code developed by Cowan [33] that is based on the multiconfiguration Hartree-Fock method. Relativistic effects are included in the Schrödinger equation as proposed by Cowan [33]. The present calculations were performed, including intermediate coupling and configuration interaction, taking into account the configurations $1s^2$, $1s2s$, $1s2p$, $1s3s$, $1s3p$, $1s3d$, $1s4s$, $1s4p$, $1s4d$, $1s4f$, $1s5s$, $1s5p$, $1s5d$, $1s5f$, $1s5g$, $1s6s$, $1s6p$, $1s6d$, $1s6f$, $1s6g$, and $1s6h$. No scaling parameters have been employed for the interaction integrals. The precision of x-ray wavelengths for the present K-shell transitions is estimated to be about 2 mÅ; transition probabilities are precise to about 20%. However, transitions in the fine structure are much less precise: Transition energies may differ by a factor of 2 and corresponding oscillator strengths up to 50%.

The third method, FAC, employs the code developed by Gu [34]. The radial orbitals for the construction of the basis states are derived from a modified self-consistent Dirac-Fock-Slater iteration on a fictitious mean configuration with fractional occupation numbers, representing the average electron cloud of the configurations included in the calculations. The radiative transition rates and matrix elements are calculated in the single multipole approximation with arbitrary rank. The present calculations were performed, including intermediate coupling and configuration interactions. The following configurations are taken into account: $1s^2$, $1s2s$, $1s2p$, $1s3s$, $1s3p$, $1s3d$, $1s4s$, $1s4p$, $1s4d$, $1s4f$, $1s5s$, $1s5p$, $1s5d$, $1s5f$, $1s5g$, $1s6s$, $1s6p$, $1s6d$, $1s6f$, $1s6g$, and $1s6h$. Wave-function optimization has been performed on state $1s^2$, Breit corrections are included for all states. The precision of x-ray wavelengths is strongly configuration and code-option dependent. For the present simulations, the precision of K-shell transitions is estimated to be about 3 mÅ; transition probabilities are precise to about 10%. However, transitions in the fine structure are much less precise: Transition energies may differ up to about 50% and corresponding oscillator strengths up to 30%.

The last method, MZ, employs a code developed by Vainshtein and Safronova [35] and Shevelko and Vainshtein [36] that is based on a multiconfiguration Z expansion. High-n and continuum states are included via hydrogenic wave functions that are summed up in an analytic procedure; more details are described in Refs. [35,36]. Relativistic effects are included via the Breit Hamiltonian; Lamb shift and vacuum polarization are also included. It was discovered long ago that this method provided excellent agreement with wavelengths' measurements even for multiple excited autoionizing states [22,37,38]. The precision of x-ray wavelengths for the present K-shell transitions is estimated to be better than about 0.5 mÅ; transition probabilities are precise to about 5%. Unfortunately, the various Z-expansion coefficients are not implemented in a general manner to treat any type of configuration, such as the case for MCDFGME, HFR, and FAC.

Table I shows a selection of different transitions in He-like aluminum that are important for the present investigations. The first six lines depict the x-ray transitions to the ground state. As every code provides slightly different values for the He-like resonance line $\mathrm{He}_\beta = 1s3p\ ^1P_1\text{-}1s^2\ ^1S_0$, the second values depict the relative differences (in units of 10^{-13} m) from the selected x-ray transition and the respective He_β transition [whereas, a full comparison of MCDFGME with the NIST data is provided in Table II(a) to be discussed below]. This difference is important for the final broadening of the He_β emission as the Stark effect induces x-ray transitions to the ground state from the $1s3d$ and $1s3s$ states, see Fig. 1. The comparison indicates that the relative energy-level positions in the fine structure between MCDFGME and MZ is excellent, whereas, for HFR and FAC (apart from absolute differences for the He_β wavelength), important differences are encountered. As concerns the levels $1s3p\ ^3P_1$ and $1s3p\ ^1P_1$, they also do allow comparison with experimental data via the observable transitions $1s3p\ ^1P_1\text{-}1s^2\ ^1S_0$ (No. 3 in Table I) and $1s3p\ ^3P_1\text{-}1s^2\ ^1S_0$ (No. 4 in Table I). NIST indicates an energy difference of $\Delta E_{\mathrm{NIST}}(1s3p\ ^1P_1\text{-}1s3p\ ^3P_1) = 2.791$ eV, MCDFGME provides $\Delta E_{\mathrm{MCDFGME}}(1s3p\ ^1P_1\text{-}1s3p\ ^3P_1) = 2.816$ eV that is in excellent agreement (relative error of only 0.90%), whereas, $\Delta E_{\mathrm{HFR}}(1s3p\ ^1P_1\text{-}1s3p\ ^3P_1) = 2.896$ eV (relative error of 3.8%) and $\Delta E_{\mathrm{FAC}}(1s3p\ ^1P_1\text{-}1s3p\ ^3P_1) = 2.921$ eV (relative error of 4.7%) indicate a precision that is worse by a factor of about 4 to 5. Only MZ is also in excellent agreement: $\Delta E_{\mathrm{MZ}}\ (1s3p\ ^1P_1\text{-}1s3p\ ^3P_1) = 2.795$ eV (relative error of only 0.14%).

The total differences in the fine structure relevant to Stark broadening are visualized in Fig. 2, that compares the line broadening calculations for the data sets MCDFGME, HFR, and FAC (note that no simulation for MZ is presented as the code did not allow for obtaining a complete set of energies and transition matrix elements for all states $1snl$ with $n = 1$–6 and $l = 0$–5). For better visualization, the calculations have been shifted and peak normalized to the line center of the He_β transition of MCDFGME. Figure 2 discovers that deviations are particularly large for states involving d-wave functions. This suggests that not only the relative x-ray energies are the subjects of "re-investigation" for the line broadening, but also all matrix elements and wavelengths in the fine structure [see also Eq. (6)].

Lines 7–12 of Table I depict transitions inside the $1s3l$ fine structure. As suggested above, the deviations for states involving d-wave functions are rather large. For example, the MCDFGME oscillator strength $f(1s3p\ ^1P_1 - 1s3d\ ^1D_2)$ (No. 10) is 25% smaller than HFR and 30% smaller than FAC; the

TABLE II. Recommended complete set of fully relativistic data for Stark profile simulations, (a) atomic states of the configurations $1s^2$, $1s2l$, and $1s3l$, energy levels E (unit of eV) are counted from the ground state, J is the total angular momentum, e = even parity, and o = odd parity. The column designated with NIST indicates the energy levels proposed by the NIST database [15–20]. (b) Dipole matrix elements (units of $e^2a_0^2$), wavelengths (units of Å), and oscillator strengths.

Number	Level	$2J+1$	Parity	E	NIST	$\Delta E(E-\text{NIST})$
1	$1s2\ ^1S_0$	1	e	0.000	0.0000	0.000
2	$1s2s\ ^3S_1$	3	e	1574.752	1574.9787	−0.23
3	$1s2p\ ^3P_0$	1	o	1587.824	1587.9705	−0.15
4	$1s2p\ ^3P_1$	3	o	1587.976	1588.1244	−0.15
5	$1s2p\ ^3P_2$	5	o	1588.608	1588.7598	−0.15
6	$1s2s\ ^1S_0$	1	e	1588.899	1588.9516	−0.05
7	$1s2p\ ^1P_1$	3	o	1598.240	1598.2902	−0.05
8	$1s3s\ ^3S_1$	3	e	1862.032	1862.3000	−0.27
9	$1s3p\ ^3P_0$	1	o	1865.627	1865.8683	−0.24
10	$1s3p\ ^3P_1$	3	o	1865.675	1865.9167	−0.24
11	$1s3s\ ^1S_0$	1	e	1865.793	1865.9939	−0.20
12	$1s3p\ ^3P_2$	5	o	1865.862	1866.1049	−0.24
13	$1s3d\ ^3D_1$	3	e	1867.802	1868.0683	−0.27
14	$1s3d\ ^3D_2$	5	e	1867.809	1868.0740	−0.27
15	$1s3d\ ^3D_3$	7	e	1867.877	1868.1437	−0.27
16	$1s3d\ ^1D_2$	5	e	1867.982	1868.2398	−0.26
17	$1s3p\ ^1P_1$	3	o	1868.491	1868.7072	−0.22

Low	Up	Matrix element	Oscillator strength	Wavelength
16	17	-1.136×10^{0}	3.222×10^{-3}	2.4354×10^{4}
14	17	3.299×10^{-1}	3.636×10^{-4}	1.8178×10^{4}
13	17	-3.244×10^{-2}	5.920×10^{-6}	1.8002×10^{4}
11	17	1.059×10^{0}	7.416×10^{-2}	4.5968×10^{3}
8	17	-5.806×10^{-2}	1.777×10^{-4}	1.9198×10^{3}
6	17	-2.399×10^{-1}	3.941×10^{-1}	4.4345×10^{1}
2	17	1.200×10^{-2}	3.426×10^{-4}	4.2209×10^{1}
1	17	-5.740×10^{-2}	1.505×10^{-1}	6.6355×10^{0}
12	16	-1.931×10^{-1}	3.872×10^{-4}	5.8496×10^{3}
10	16	2.724×10^{-1}	1.398×10^{-3}	5.3748×10^{3}
7	16	-5.408×10^{-1}	6.439×10^{-1}	4.5964×10^{1}
5	16	8.848×10^{-2}	1.070×10^{-2}	4.4379×10^{1}
4	16	-1.266×10^{-1}	3.661×10^{-2}	4.4279×10^{1}
12	15	1.406×10^{0}	1.953×10^{-2}	6.1527×10^{3}
5	15	-6.450×10^{-1}	5.688×10^{-1}	4.4396×10^{1}
12	14	-5.620×10^{-1}	3.012×10^{-3}	6.3693×10^{3}
10	14	9.932×10^{-1}	1.719×10^{-2}	5.8105×10^{3}
7	14	1.590×10^{-1}	5.572×10^{-2}	4.5994×10^{1}
5	14	2.578×10^{-1}	9.092×10^{-2}	4.4407×10^{1}
4	14	-4.540×10^{-1}	4.708×10^{-1}	4.4306×10^{1}
12	13	1.534×10^{-1}	2.236×10^{-4}	6.3912×10^{3}
10	13	-5.933×10^{-1}	6.115×10^{-3}	5.8287×10^{3}
9	13	6.862×10^{-1}	2.508×10^{-2}	5.7017×10^{3}
7	13	1.440×10^{-2}	4.596×10^{-4}	4.5995×10^{1}
5	13	-7.035×10^{-2}	6.774×10^{-3}	4.4408×10^{1}
4	13	2.716×10^{-1}	1.685×10^{-1}	4.4308×10^{1}
3	13	-3.139×10^{-1}	6.755×10^{-1}	4.4284×10^{1}
8	12	1.353×10^{0}	5.722×10^{-2}	3.2375×10^{3}
2	12	-2.967×10^{-1}	2.091×10^{-1}	4.2590×10^{1}
10	11	5.741×10^{-2}	3.194×10^{-6}	1.0447×10^{5}
7	11	8.771×10^{-2}	1.680×10^{-2}	4.6340×10^{1}
4	11	-3.885×10^{-3}	3.396×10^{-5}	4.4628×10^{1}
8	10	-1.045×10^{0}	3.251×10^{-2}	3.4039×10^{3}
6	10	1.381×10^{-2}	1.302×10^{-3}	4.4796×10^{1}
2	10	2.302×10^{-1}	1.259×10^{-1}	4.2618×10^{1}
1	10	3.082×10^{-3}	4.546×10^{-4}	6.6455×10^{0}
8	9	6.044×10^{-1}	1.072×10^{-2}	3.4488×10^{3}

TABLE II. (*Continued.*)

Low	Up	Matrix element	Oscillator strength	Wavelength
2	9	-1.332×10^{-1}	4.216×10^{-2}	4.2624×10^{1}
7	8	5.074×10^{-3}	5.582×10^{-5}	4.7001×10^{1}
5	8	1.142×10^{-1}	1.747×10^{-2}	4.5345×10^{1}
4	8	8.767×10^{-2}	1.719×10^{-2}	4.5240×10^{1}
3	8	5.059×10^{-2}	1.718×10^{-2}	4.5215×10^{1}
6	7	4.329×10^{-1}	4.289×10^{-2}	1.3273×10^{3}
2	7	-2.219×10^{-2}	9.443×10^{-5}	5.2786×10^{2}
1	7	-1.378×10^{-1}	7.423×10^{-1}	7.7575×10^{0}
4	6	2.154×10^{-2}	3.498×10^{-6}	1.3425×10^{4}
2	5	5.484×10^{-1}	3.403×10^{-2}	8.9478×10^{2}
2	4	-4.237×10^{-1}	1.939×10^{-2}	9.3758×10^{2}
1	4	7.021×10^{-3}	2.000×10^{-3}	7.8077×10^{0}
2	3	2.449×10^{-1}	6.402×10^{-3}	9.4844×10^{2}

MCDFGME wavelength $\lambda(1s3p\ ^1P_1 - 1s3d\ ^1D_2)$ is 30% larger than HFR and 40% larger than FAC. Moreover, the energy differences of MCDFGME are in much better agreement with NIST than the case for HFR and FAC. For example, for the transition $1s3d\ ^1D_2$-$1s3p\ ^1P_1$ (No. 10 in Table I), the MCDFGME wavelength deviates only 8% from NIST and only 7% for the transition $1s3d\ ^3D_2$-$1s3p\ ^1P_1$ (No. 12 in Table I), whereas, HFR deviates by 30% and 24% for these transitions, and FAC deviates by 34% and 43%.

III. STARK BROADENING STUDIES OF He_β

Due to the large number of transitions, it is difficult to estimate the impact for the line broadening from the table-data comparison. Figure 3(a) shows, therefore, the He_β broadening for different data for an electron density of 10^{22} cm^{-3} and an electron temperature of $kT_e = 100$ eV. It is easily observed that all maxima are quite different for different data sets. Figure 3(b) shows the same calculations, such as in Fig. 3(a), however, HFR and FAC have been shifted and have been scaled to peak intensity of the He_β transitions MCDFGME.

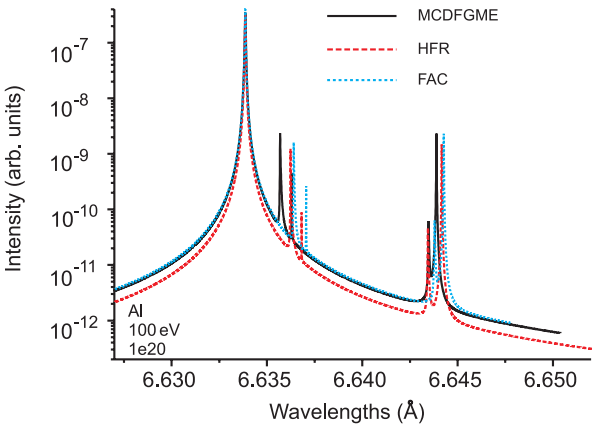

FIG. 2. (Color online) He_β Stark profile of aluminum for different atomic data sets: black solid curve: MCDFGME; red dashed curve: HFR; blue dotted curve: FAC; $kT_e = 100$ eV; $n_e = 10^{20}$ cm^{-3}. Simulations for different data sets have been shifted and have been normalized to the He_β peak MCDFGME.

This comparison discovers that HFR and FAC provide second maxima that are too small with separation that is too large from the He_β line that is directly related to the significant differences in atomic data depicted in Table I (in particular, related to the transition No. 10). This difference might partially explain the

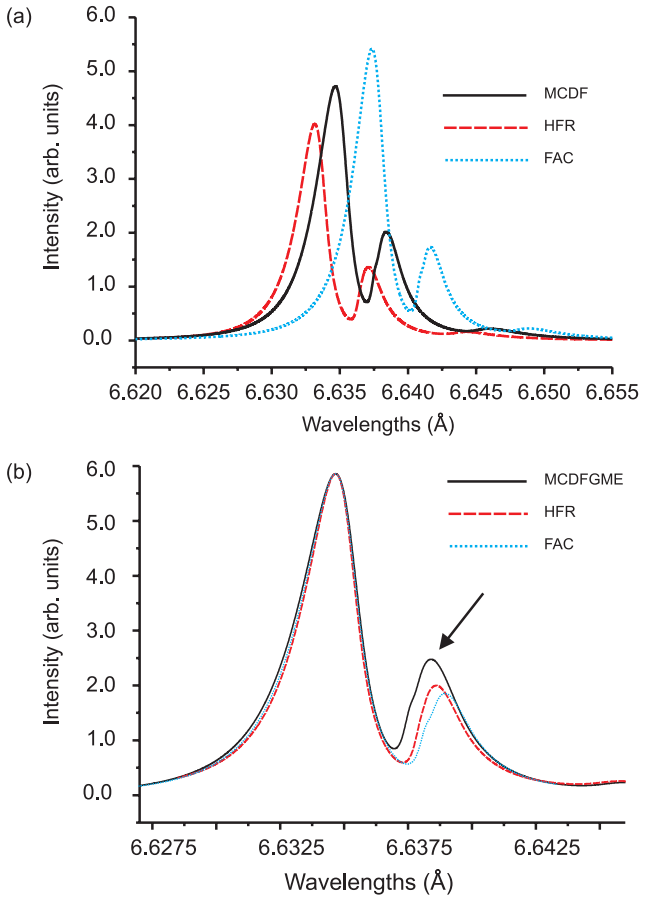

FIG. 3. (Color online) (a) Stark profile simulations of aluminum He_β employing different atomic data $kT_e = 100$ eV and $n_e = 10^{22}$ cm^{-3}. (b) The same as Fig. 1(a), however, line profiles have been shifted to the MCDFGME line center position and have been normalized to peak intensity. Large discrepancies between the different data sets are observed (indicated by the arrow).

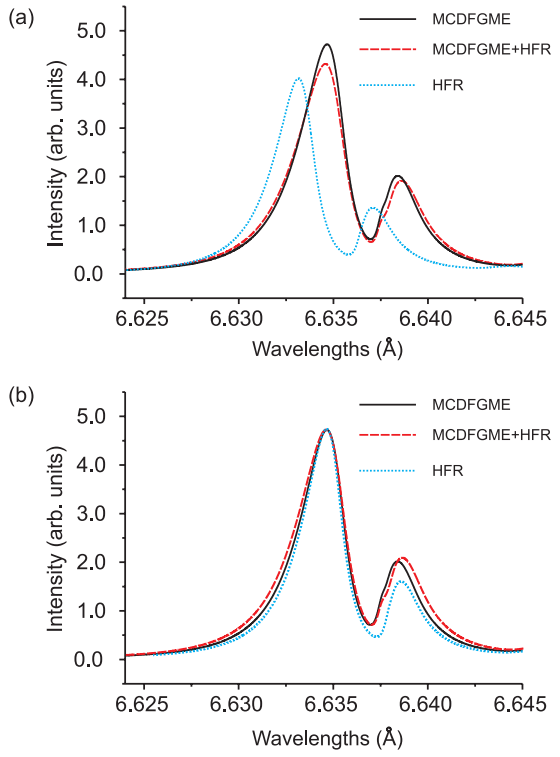

FIG. 4. (Color online) (a) He_β Stark profile of aluminum for different mixed sets of atomic data: $kT_e = 100$ eV and $n_e = 10^{22}$ cm^{-3}. Black solid curve: MCDFGME data; red dashed curve: MCDFGME data, except for the matrix element $\langle 1s3d\ ^1D_2|r|1s3p\ ^1P_1\rangle$ that employs HFR data; and blue dotted curve: HFR data. (b) The same as Fig. 3(a), however, the curves have been normalized and have been shifted to the peak intensity of MCDFGME.

often-observed discrepancy in Stark broadening analysis [6] near the line center of He_β [see also Fig. 3(b), arrow].

As the deviation of the data concerning the matrix element $\langle 1s3d\ ^1D_2|r|1s3p\ ^1P_1\rangle$ is the largest in Table I, Figs. 4(a) and 4(b) present a "mixed" calculation. The black solid curve shows pure MCDFGME data, and the red dashed curve is calculated using MCDFGME data, except for the matrix element $\langle 1s3d\ ^1D_2|r|1s3p\ ^1P_1\rangle$ where the HFR value is employed. The blue dotted curve presents pure HFR data. From the red dashed curve, it can clearly be seen that the simple exchange of this matrix element already results in rather noticeable changes in the spectral distribution and its peak intensity. Also, Fig. 4(b) suggests that the overall broadening of the He_β group is strongly related to the matrix element $\langle 1s3d\ ^1D_2|r|1s3p\ ^1P_1\rangle$.

In order to study the influence on the overall broadening for certain matrix elements, Figs. 5(a)–5(c) present a variation in different matrix elements based on the MCDFGME data set. Figure 5(a) shows a variation in $\langle 1s3d\ ^1D_2|r|1s3p\ ^1P_1\rangle$: The black solid curve presents the original MCDFGME data set, the red dashed curve employs MCDFGME data, except that the matrix element $\langle 1s3d\ ^1D_2|r|1s3p\ ^1P_1\rangle$ is replaced by $2\langle 1s3d\ ^1D_2|r|1s3p\ ^1P_1\rangle$, and the blue dotted curve also employs MCDFGME data, except that the matrix element $\langle 1s3d\ ^1D_2|r|1s3p\ ^1P_1\rangle$ is replaced by $0.5\langle 1s3d\ ^1D_2|r|1s3p\ ^1P_1\rangle$. Figure 5(a) shows that the overall line broadening and the splitting between the maxima are strongly dependent on the absolute value of the

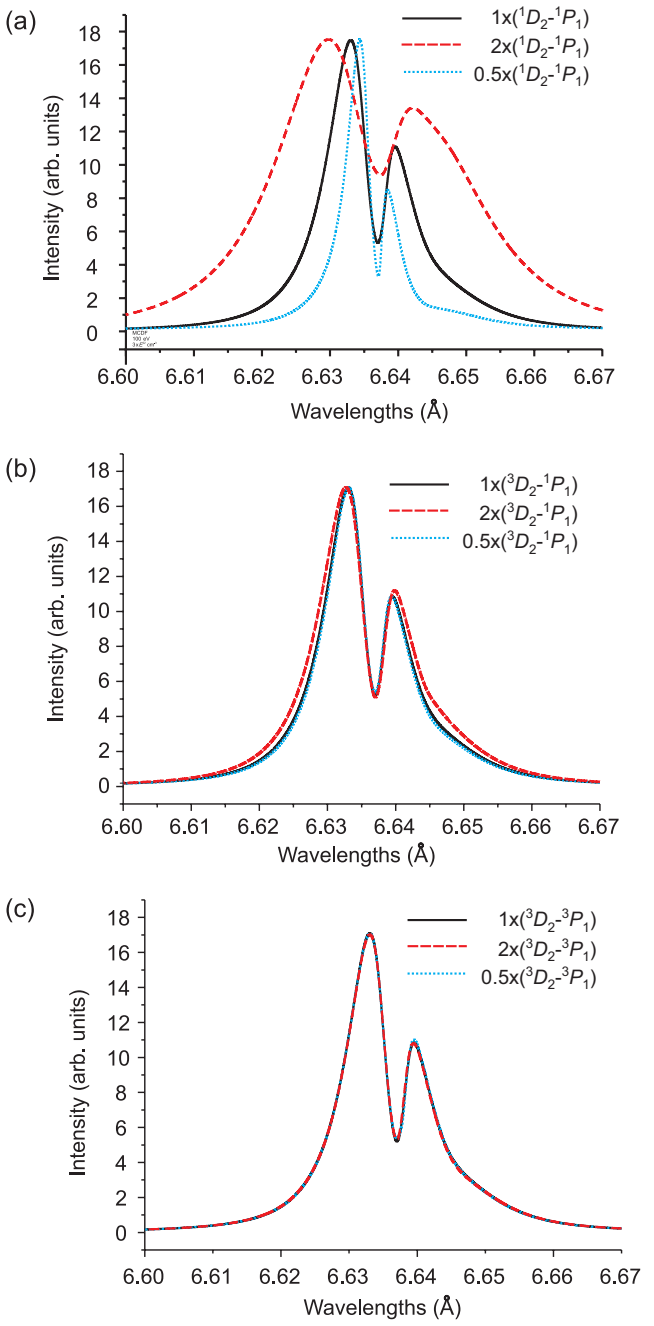

FIG. 5. (Color online) (a) Variation in the dipole matrix element $\langle 1s3d\ ^1D_2|r|1s3p\ ^1P_1\rangle$and its influence on the He_β Stark profile of aluminum for $kT_e = 100$ eV and $n_e = 3 \times 10^{22}$ cm^{-3}. All data are MCDFGME data, black solid curve: *ab initio* data set; red dashed curve: only the matrix element $\langle 1s3d\ ^1D_2|r|1s3p\ ^1P_1\rangle$ is multiplied by a factor of 2; and blue dotted curve: the matrix element is multiplied by a factor of 0.5. (b) The same as (a), however, only a variation in the intercombination dipole matrix element $\langle 1s3d\ ^3D_2|r|1s3p\ ^1P_1\rangle$is involved. (c) The same as (a), however, only a variation in the dipole matrix element of the triplet system $\langle 1s3d\ ^3D_2|r|1s3p\ ^3P_1\rangle$is involved.

$\langle 1s3d\ ^1D_2|r|1s3p\ ^1P_1\rangle$ matrix element. For the same reason, the "red dotted curve" of Fig. 4(a) has a second maximum that moves to the right because the HFR matrix element is larger than those of MCDFGME (see No. 10 in Table I).

Intermediate-coupling effects mix singlet and triplet states and might, therefore, influence the broadening. Figure 5(b) presents, therefore, a variation in the intercombination matrix element $\langle 1s3d\ ^3D_2|r|1s3p\ ^1P_1\rangle$. The red dashed curve employs MCDFGME data, except that the matrix element $\langle 1s3d\ ^3D_2|r|1s3p\ ^1P_1\rangle$ is replaced by $2\langle 1s3d\ ^3D_2|r|1s3p\ ^1P_1\rangle$, and the blue dotted curve also employs MCDFGME data, except that the matrix element $\langle 1s3d\ ^3D_2|r|1s3p\ ^1P_1\rangle$ is replaced by $0.5\langle 1s3d\ ^3D_2|r|1s3p\ ^1P_1\rangle$. The red dashed curve shows that an increase in this matrix element results in a noticeable increase in the overall broadening. This discovers that intermediate-coupling effects $[\Psi(1s3d\ ^3D_2) \approx 0.957\ 84\Psi^{LS}(1s3d\ ^3D_2) + 0.287\ 30\Psi^{LS}(1s3d\ ^1D_2)]$ may seriously influence the line broadening. For the present configurations, however, the effect is not pronounced very much. Note that the atomic data, depicted in Table I (No. 12), differ very much from each other, however, their absolute importance for the Stark effect (last column of Table I) is much lower than, e.g., for No. 10. The overall effect on the line profile is, therefore, reduced.

Figure 5(c) shows a variation in the matrix element in the triplet system $\langle 1s3d\ ^3D_2|r|1s3p\ ^3P_1\rangle$. The black solid curve presents the original MCDFGME data set, the red dashed curve equally employs all MCDFGME data, except that the matrix element $\langle 1s3d\ ^3D_2|r|1s3p\ ^3P_1\rangle$ is replaced by $2\langle 1s3d\ ^3D_2|r|1s3p\ ^3P_1\rangle$, and the blue dotted curve also employs MCDFGME data, except that the matrix element $\langle 1s3d\ ^3D_2|r|1s3p\ ^3P_1\rangle$ is replaced by $0.5\langle 1s3d\ ^3D_2|r|1s3p\ ^3P_1\rangle$. Figure 5(c) demonstrates that a variation in the matrix elements in the triplet system has no strong influence on the broadening for He_β, but this might also be different for other configurations.

Figure 6 presents a variation in fine-structure energies. The black solid curve presents the original MCDFGME data set. The red dashed curve shows a calculation where the energy difference between states $1s3d\ ^1D_2$ and $1s3p\ ^1P_1$, namely $\Delta E = E(1s3p\ ^1P_1) - E(1s3d\ ^1D_2) > 0$ has been increased by a factor of 2, i.e., $E(1s3p\ ^1P_1)$ is replaced by $E(1s3p\ ^1P_1) + \Delta E$. The blue dotted curve shows a calculation where this energy difference is decreased by a factor of 2, i.e., $E(1s3p\ ^1P_1)$ is replaced by $E(1s3p\ ^1P_1) - 0.5\ \Delta E$. An important observation is made from this calculation (Fig. 6): The intensity peak of the second maximum is strongly dependent on the energy difference $\Delta E = E(1s3p\ ^1P_1) - E(1s3d\ ^1D_2)$; if the energy difference is smaller, the second maxima have a relatively higher intensity. This correlates with the data depicted in Table I. As shown by Fig. 5, one of the most important transitions for the electric-field effects seems to be No. 10: The wavelengths of the present MCDFGME is considerably larger (means a lower transition energy) than those of FAC and HFR, whereas, FAC and HFR are very similar. This might be the reason why the second maximum is higher for MCDFGME than for FAC and HFR.

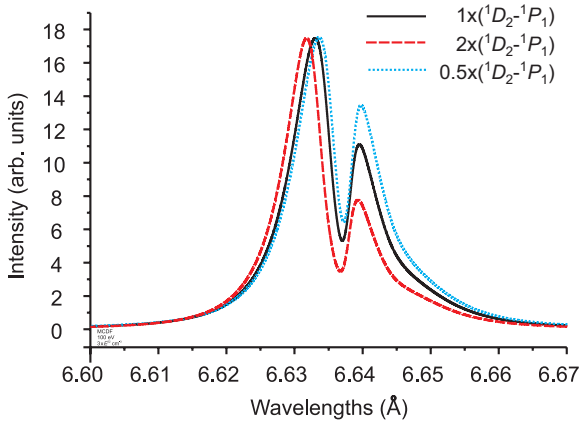

FIG. 6. (Color online) Variation in the $1s3l$ fine-structure energies and their influence on the He_β Stark profile of aluminum for $kT_e = 100$ eV and $n_e = 3 \times 10^{22}$ cm^{-3}. All data are MCDFGME data, black solid curve: *ab initio* data set; red dashed curve: the energy difference between states $1s3p\ ^1P_1$ and $1s3d\ ^1D_2$ has been increased by a factor of 2; and blue dotted curve: the energy difference between states $1s3p\ ^1P_1$ and $1s3d\ ^1D_2$ has been decreased by a factor of 2.

We note that the increase in the energy difference also results in a slight blueshift of the whole He_β group, the decrease in a slight redshift (Fig. 6). These shifts, however, seem to be much less important that those induced by oscillator strength variations as presented in Fig. 5(a). Also, they are of different origins, and comparison is limited.

Figures 5 [in particular, Fig. 5(a)] and 6 indicate that different second maxima are the combined effects of different energy levels (relative difference of the fine-structure levels) and oscillator strength (of transitions within the fine structure).

IV. COMMENTS ON RELATIVISTIC EFFECTS

As the present MCDFGME method provides a fully relativistic approach to calculate atomic structure, the nonrelativistic case can be studied setting $c \to \infty$. We discover the surprising result that in this limit, $f_{E1}(1s3d\ ^1D_2 - 1s3p\ ^1P_1)_{c\to\infty}^{\mathrm{MCDFGME}} = 4.66 \times 10^{-3}$ ($f_{E1}(1s3d\ ^1D_2 - 1s3p\ ^1P_1)_c^{\mathrm{MCDFGME}} = 3.22 \times 10^{-3}$) is close to the values provided by the methods FAC ($f_{E1}(1s3d\ ^1D_2 - 1s3p\ ^1P_1)^{\mathrm{FAC}} = 4.58 \times 10^{-3}$) and HFR($f_{E1}(1s3d\ ^1D_2 - 1s3p\ ^1P_1)^{\mathrm{HFR}} = 4.28 \times 10^{-3}$), see Table I. In order to study the relativistic effects on the final line profile, Fig. 7 presents the simulations for MCDFGME, MCDFGME nonrelativistic, FAC, and HFR for a density of $n_e = 10^{20}$ cm^{-3}. Apart from a general shift in the whole He_β emission, MCDFGME, FAC, and HFR provide a clear level splitting in the fine structure that is visible via the Stark transitions $1s3d$-$1s^2\ ^1S_0$ and $1s3s$-$1s^2\ ^1S_0$ (see the discussion related to Fig. 1). This indicates that fine-structure splitting effects are reasonably well described by FAC and HFR, whereas, the MCDFGME nonrelativistic does not show a reasonable splitting. At higher densities, however, these effects appear to be of minor importance. This is demonstrated with Fig. 8 that shows the case for $n_e = 10^{22}$ cm^{-3} and $kT_e = 100$ eV. From the normalized presentation of Fig. 8(b), it can clearly be seen that the MCDFGME nonrelativistic is very close to FAC and HFR simulations, whereas, the fully relativistic approach of MCDFGME is different from all curves. This indicates that the complete implementation of relativistic effects in the MCDFGME approach [23–31] is very important and strongly shows up in visible effects for the Stark broadening even on a linear intensity scale.

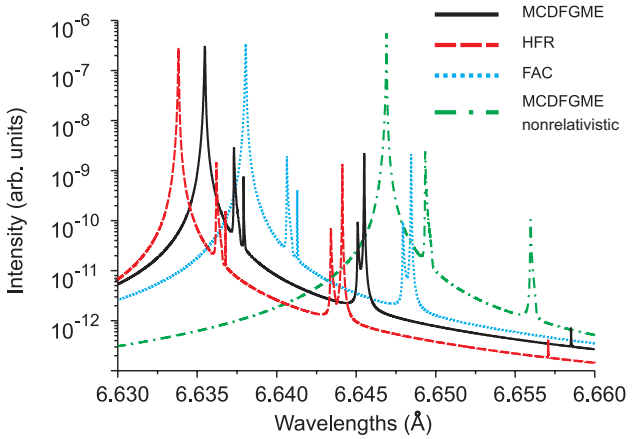

FIG. 7. (Color online) Influence of relativistic effects on the He_β Stark profile of aluminum for different atomic data sets: black solid curve: MCDFGME; green dot-dashed curve: "MCDFGME nonrelativistic;" red dashed curve: HFR; and blue dotted curve: FAC, $kT_e = 100$ eV and $n_e = 10^{20}$ cm^{-3}.

V. COMPLETE RELATIVISTIC DATA SET FOR STARK PROFILE CALCULATIONS

In order to provide a reference set of atomic data for Stark profile calculations, Tables II(a) and II(b) list all energy levels and possible electric-dipole transitions (wavelengths, matrix elements with signs, and oscillator strengths) for the $1s^2$, $1s2l$, and $1s3l$ configurations. Table II(a) shows the definition of energy levels that are designated according to the LS-coupling scheme. The first column is a running number for the energy levels, the second column specifies the level in spectroscopic notation, the third column indicates the statistical weight, the fourth column indicates the parity, the fifth column indicates the energy in (eV) counted from the ground state (zero energy) for the present MCDFGME calculations, in the sixth column are the energy levels from NIST [15,20], and the last column indicates the differences between the MCDFGME and the NIST data. The last column indicates a systematic shift of about -0.2 eV for the $1s3l$ levels. We are particularly interested in the energy precision of the different fine-structure levels relative to each other. For the important transition $1s3d\ ^1D_2 - 1s3p\ ^1P$ [see Figs. 5(a) and 6 and the related discussion in the text], the agreement is within 0.04 eV, indicating a relative precision of the fine-structure energy levels of about 8%. As indicated by Figs. 5(a) and 6, 10% variations in energy levels and oscillator strengths within the fine structure seem to not have an overall great influence on the line shapes. It should be recalled here that the difference in wavelength between FAC and MCDFGME (see Nos. 10 and 12 in Table I) is about 40% and, compared to HFR, is about 30% (see also discussion in Sec. II).

Table II(b) shows data relevant to the transitions. The first column indicates the number of the lower atomic level, the second column is the number of the upper atomic level, the third column shows the dipole matrix elements, including the signs in units of ea_0, the fourth column shows the oscillator strengths, and the fifth column shows the transition wavelengths in angstroms. We note that, e.g., the wavelengths of the He-like resonance transition $1s2p\ ^1P_1 - 1s^2\ ^1S_0$ is

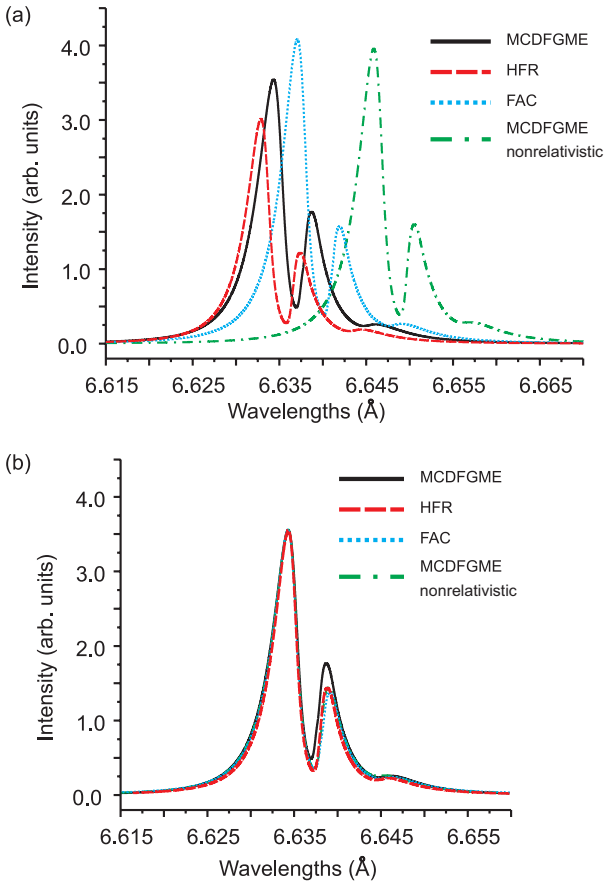

FIG. 8. (Color online) (a) Influence on the He_β Stark profile of aluminum for different atomic data sets: black solid curve: MCDFGME; green dot-dashed curve: MCDFGME nonrelativistic; red dashed curve: HFR; and blue dotted curve: FAC; $kT_e = 100$ eV; $n_e = 10^{22}$ cm^{-3}. (b) The same as (a), however, all calculations have been shifted and have been normalized to MCDFGME data.

predicted by our present calculations to be at $\lambda_{\text{MCDFGME}} = 7.7575$ Å, whereas, the NIST data [15,17] provide an observed wavelength of $\lambda_{\text{observed}} = 7.7575$ Å, indicating excellent agreement. For the intercombination transition $1s2p\ ^3P_1 - 1s^2\ ^1S_0$, $\lambda_{\text{MCDFGME}} = 7.8078$ Å, whereas, $\lambda_{\text{observed}} = 7.8069$ Å [15,17]. Comparisons for the transitions $1s3p\ ^1P_1 - 1s^2\ ^1S_0$ and $1s3p\ ^3P_1 - 1s^2\ ^1S_0$ are provided in Table I. The agreement between the present calculations and the observed data [15,18] is very good, and the transition probabilities are in excellent agreement (almost identical) with the NIST data [15,16].

The data in Table II will provide an important benchmark set of atomic constants that not only may be employed for the Stark profile calculation itself, but also may be employed to study various different effects in Stark broadening theory, such as, e.g., interference effects [4,12–14,39], microfield approximations [40,41], and frequency fluctuation methods [8,9]).

VI. CONCLUSION

A critical analysis of different calculation methods of fine-structure energies and matrix elements for applications in line broadening theory has been provided. The He_β

x-ray transition of highly charged ions that is frequently employed for Stark broadening analysis in dense plasmas has been studied as a test case. Despite its simple atomic structure, strong deviations are demonstrated when employing different methods and codes of calculation that are widely used in the community. As current atomic databases do not provide data relevant to Stark broadening, we have performed corresponding benchmark simulations based on an advanced multi-configuration-Dirac-Fock approach to provide a complete reference data set. The fully relativistic approach of the present MCDFGME method discovers visible deviations for line broadening calculations compared to the case when standard relativistic approximations are employed.

A complete reference data set, comprising all relevant energies and electric-dipole matrix elements in the intermediate-coupling scheme for Stark profile simulations of all transitions within the $1s^2$, $1s2l$, and $1s3l$ configurations (e.g., He_α, He_β, and H_α), is presented.

ACKNOWLEDGMENTS

This research was supported, in part, by FCT Projects No. Pest-OE/FIS/UI0303/2011 and No. PTDC/FIS/117606/2010, the "Extreme Matter Institute EMMI," the project "Emergence-2010" of the University Pierre and Marie Curie, and the Program Hubert Curien PESSOA 20022VB.

[1] H. R. Griem, *Plasma Spectroscopy* (McGraw-Hill, New York, 1964).
[2] H. R. Griem, *Spectral Line Broadening by Plasma* (Academic, New York, 1974).
[3] H. R. Griem, *Principles of Plasma Spectroscopy* (Cambridge University Press, New York, 1997).
[4] I. I. Sobelman, L. A. Vainshtein, and E. A. Yukov, *Excitation of Atoms and Broadening of Spectral Lines* (Springer, Berlin, 1995).
[5] L. A. Woltz, V. L. Jacobs, C. F. Hooper, and R. C. Mancini, Phys. Rev. A **44**, 1281 (1991).
[6] N. C. Woolsey, A. Asfaw, B. Hammel, C. Keane, C. A. Back, A. Calisti, C. Mossé, R. Stamm, B. Talin, J. S. Wark, R. W. Lee, and L. Klein, Phys. Rev. E **53**, 6396 (1996).
[7] A. Calisti, F. Khelfaoui, R. Stamm, B. Talin, and R. W. Lee, Phys. Rev. A **42**, 5433 (1990).
[8] B. Talin, A. Calisti,L. Godbert, R. Stamm, R. W. Lee, and L. Klein, Phys. Rev. A **51**, 1918 (1995).
[9] B. Talin, A. Calisti, S. Ferri, M. Koubiti, T. Meftah, C. Mossé, L. Mouret, R. Stamm, S. Alexiou, R. W. Lee, and L. Klein, J. Quant. Spectrosc. Radiat. Transfer **58**, 953 (1997).
[10] A. Calisti, S. Ferri, C. Mossé-Sabonnadière, and B. Talin, report no 1, Université de Provence, Marseille, France, 2006.
[11] A. Calisti, C. Mossé, S. Ferri, B. Talin, F. Rosmej, L. A. Bureyeva, and V. S. Lisitsa, Phys. Rev. E **81**, 016406 (2010).
[12] F. B. Rosmej, in *Handbook for Highly Charged Ion Spectroscopic Research*, edited by Y. Zou and R. Hutton (Taylor & Francis, Boca Raton, FL, 2012), p. 267.
[13] F. B. Rosmej, in *Free Electron Laser*, edited by S. Varró (InTech, Rijeka, Croatia, 2012), p. 187.
[14] E. Galtier, F. B. Rosmej, A. Calisti, B. Talin, C. Mossé, S. Ferri, and V. S. Lisitsa, Phys. Rev. A, accepted for publication.
[15] A. Kramida, Yu. Ralchenko, J. Reader, and NIST ASD Team, *NIST Atomic Spectra Database* (version 5.0), online (2012). Available at the National Institute of Standards and Technology, Gaithersburg, MD (2013), http://physics.nist.gov/asd
[16] F. Khan, G. S. Khandelwal, and J. W. Wilson, Astrophys. J. **329**, 493 (1988).
[17] X. C. Martin, Phys. Scr. **24**, 725 (1981).
[18] V. A. Boiko, A. Y. Faenov, S. A. Pikuz, I. Y. Skobelev, A. V. Vinogradov, and E. A. Yukov, J. Phys. B **10**, 3387 (1977).
[19] D. E. Kelleher and L. I. Podobedova, J. Phys. Chem. Ref. Data **37**, 709 (2008).
[20] W. C. Martin and R. Zalubas, J. Phys. Chem. Ref. Data **8**, 817 (1979).
[21] F. B. Rosmej, A. Y. Faenov, T. A. Pikuz, F. Flora, P. Di Lazzaro, S. Bollanti, N. Lizi, T. Letardi, A. Reale, L. Palladino, O. Batani, S. Bossi, A. Bornardinello, A. Scafati, and L. Reale, J. Phys. B **31**, L921 (1998).
[22] F. B. Rosmej, A. Calisti, B. Talin, R. Stamm, D. H. H. Hoffmann, W. Süß, M. Geißel, A. Y. Faenov, and T. A. Pikuz, J. Quant. Spectrosc. Radiat. Transfer **71**, 639 (2001).
[23] J. P. Desclaux, Comput. Phys. Commun. **9**, 31 (1975).
[24] MCDFGME, a multiconfiguration Dirac-Fock and general matrix elements program, edited by J. P. Desclaux and P. Indelicato (2011), http://dirac.spectro.jussieu.fr/mcdf
[25] J. P. Desclaux, in *Methods and Techniques in Computational Chemistry, Small Systems of METTEC*, edited by E. Clementi, Vol. A (STEF, Cagliari, 1993), p. 253.
[26] P. Indelicato, Phys. Rev. A **51**, 1132 (1995).
[27] P. Indelicato, Phys. Rev. Lett. **77**, 3323 (1996).
[28] O. Gorceix, P. Indelicato, and J. P. Desclaux, J. Phys. B **20**, 639 (1987).
[29] P. Indelicato, O. Gorceix, and J. P. Desclaux, J. Phys. B **20**, 651 (1987).
[30] P. Indelicato, Nucl. Instrum. Methods Phys. Res. B **31**, 14 (1988).
[31] P. Indelicato, F. Parente, and R. Marrus, Phys. Rev. A **40**, 3505 (1989).
[32] P. O. Löwdin, Phys. Rev. **97**, 1474 (1955).
[33] R. D. Cowan, *Theory of Atomic Structure and Spectra* (University of California Press, Berkeley, 1981).
[34] M. F. Gu, Can. J. Phys. **86**, 675 (2008).
[35] L. A. Vainshtein and U. I. Safronova, Phys. Scr. **31**, 519 (1985).
[36] V. P. Shevelko and L. A. Vainshtein, *Atomic Physics for Hot Plasmas* (IOP, Bristol, 1993).
[37] L. A. Vainshtein and U. I. Safronova, At. Data Nucl. Data Tables **21**, 49 (1978).
[38] F. F. Goryayev, A. M. Urnov, and L. A. Vainshtein, report 9 March 2007, Lebedev Physical Technical Institute, Moscow, 2007.
[39] V. A. Aleseyev and I. I. Sobelman, Sov. Phys. JETP **28**, 991 (1969).
[40] C. A. Iglesias, J. L. Lebowitz, and D. MacGowan, Phys. Rev. A **28**, 1667 (1983).
[41] D. P. Kilcrease, R. C. Mancini, and C. F. Hooper, Jr., Phys. Rev. E **48**, 3901 (1993).